Research Square

Preprints are preliminary reports that have not undergone peer review.
They should not be considered conclusive, used to inform clinical practice,
or referenced by the media as validated information.

Topology-Aware Trigonometric Barrier Geometry for Safety-Margin Robot Motion Planning on Periodic Configuration Spaces

Mona Hamad Alzanbagi

malzanbagi@kau.edu.sa

King Abdulaziz University

Lamis M. Alamoudi

King Abdulaziz University

Article

Keywords: Trigonometric robotics, periodic configuration spaces, torus-consistent motion planning, tangent barrier functions, singularity avoidance, angular wrap-around correction, robot trajectory diagnostics

Posted Date: June 12th, 2026

DOI: https://doi.org/10.21203/rs.3.rs-9773636/v1

License: This work is licensed under a Creative Commons Attribution 4.0 International License.
Read Full License

Additional Declarations: No competing interests reported.

Topology-Aware Trigonometric Barrier Geometry for Safety-Margin Robot Motion Planning on Periodic Configuration Spaces

Mona Hamad Alzanbagi[1,*], Lamis M. Alamoudi[2]
[1]Faculty of Science, Department of Statistics, King Abdulaziz University, Jeddah, Saudi Arabia
malzanbagi@kau.edu.sa
[2]Faculty of Science, Department of Statistics, King Abdulaziz University, Jeddah, Saudi Arabia
lalamodi@kau.edu.sa

*Corresponding Author Email: malzanbagi@kau.edu.sa

Abstract: Robotic manipulators with revolute joints evolve on periodic configuration spaces, but many planning and trajectory-analysis pipelines still evaluate angular motion through Euclidean coordinate differences. This mismatch can introduce branch-cut discontinuities and distort path length, smoothness, and safety-margin assessment near angular wrap-around boundaries. This paper develops a topology-aware trigonometric barrier geometry for safety-margin motion planning on periodic configuration spaces. Angular coordinates are represented by sine-cosine embeddings, trajectory smoothness is measured by a torus-consistent chordal distance, and tangent-barrier terms penalize approach to obstacle-clearance, joint-limit, and Jacobian-singularity boundaries. The resulting functional is quotient-consistent under angular representative changes, smooth in the safe interior, divergent at unsafe boundaries, and stable under bounded perturbations away from the boundary. A finite candidate-search planner with edge-sampled admissibility checks and an online safety-filter formulation implements the framework. Controlled simulations compare Euclidean, trigonometric-only, barrier-only, and full trigonometric-barrier planners. The full planner succeeds in the coupled constrained scenario, while DROID-100 diagnostics show a 5.896-fold Euclidean path inflation relative to the shortest-periodic trigonometric representation. These results support trigonometric barrier geometry as a mathematically consistent planning and diagnostic layer for periodic robotic systems.

Keywords: Trigonometric robotics; periodic configuration spaces; torus-consistent motion planning; tangent barrier functions; singularity avoidance; angular wrap-around correction; robot trajectory diagnostics

1. Introduction

Research into robot motion planning has recently shifted its focus from geometric path design alone to safety-aware planning in the face of kinematic, environmental, and deployment limitations. Even though sampling-based motion planning is still the gold standard due to its ability to deal with complicated constraints and high-dimensional configuration spaces, newer evaluations have highlighted the ongoing difficulties in dealing with tight spaces, changing environments, planner selection, and unique configuration-space structures (Orthey et al., 2024; Zhang et al., 2025a).

More recent research has expanded this focus to industrial and human-centered manipulator contexts, such as the optimisation of BiRRT/B-spline trajectories for 6-DOF arms and the modification of APF-PRM planning for human-centric obstacle avoidance (Elgohr et al., 2026; Narendula et al., 2026). Since revolute joints introduce periodic coordinates, these problems become even more specific for robotic manipulators; in addition, practical implementation necessitates avoiding singularities, redundancy, obstacles, and preserving joint limits. Aydogmus & Boztas (2024), Baron et al. (2020), Hentout et al. (2023), Li et al. (2023), Secil & Ozkan (2023), and Zhang et al. (2025b) are among the many manipulator-planning studies that have tackled topics such as collision-free trajectory generation, safe human-robot interaction, redundancy-based inverse kinematics, singularity-free arm motion, and geometric singularity avoidance using optimisation, fuzzy logic, geometric methods, and learning-based

models. Although these studies highlight the significance of constraint-aware manipulation, the angular topology of revolute-joint coordinates is more often seen as a part of the modelling process than as a planning geometry that has an impact on path-length diagnostics and trajectory smoothness.

The second important base is provided by safety-critical controls. When it comes to maintaining nominal control objectives while imposing state limits, control barrier functions and safety filters have emerged as key techniques. According to recent reviews, safety filters are modular supervisory mechanisms that step in when a nominal controller is about to breach safety constraints (Hsu et al., 2024). On the other hand, control-barrier-function theory has been revised to include input constraints, high-relative-degree systems, disturbances, sampled-data effects, and implementation challenges in autonomous and robotic systems (Cohen et al., 2024; Garg et al., 2024).

Recent human–robot interaction work further shows that CBF-based controllers can prioritize safety constraints in real time when manipulators operate near moving humans (Maithani et al., 2026). Predictive safety filters and learning-based model predictive control further show how constrained dynamics, uncertainty, and online correction can be incorporated into safety-aware control pipelines (Brunke et al., 2022; Hewing et al., 2020; Wabersich & Zeilinger, 2021). Related work on learned certificates also reflects growing interest in combining data-driven control with Lyapunov, barrier, and contraction-based guarantees (Dawson et al., 2023). These developments motivate the command-level safety-filter pathway in the present study. However, most safety-filter formulations focus on constraint satisfaction in the state or control space; they do not explicitly address the topological distortion that arises when angular coordinates are measured through Euclidean subtraction across branch cuts.

Geometric collision representations are also closely related. Neural signed-distance fields, configuration-space distance fields, and robot-geometry distance representations have recently been used to support manipulation planning, perception, and reactive control (Koptev et al., 2023; Li et al., 2024a, 2024b; Ortiz et al., 2022).

When local reactive corrections or collision costs need to be factored into motion planning, these methods furnish effective means of encoding robot geometry and obstacle proximity. Researchers have shown that distance-field mapping and planning can help humans and robots work together in shared spaces safer during interactions (Ali et al., 2024). This line of research is supplemented by the present work. Prior to evaluating the clearance and barrier terms, it creates a trigonometric configuration-space geometry rather than suggesting a new signed-distance model or scene reconstruction. This difference is significant because, unless periodic coordinates are fundamentally handled, a chart-dependent angular smoothness cost can be linked with an otherwise accurate distance or barrier model.

A new reason to use topology-aware trajectory diagnostics has emerged from recent real-robot datasets. There has been a general movement away from fixed laboratory evaluation and toward heterogeneous manipulation data, and DROID is a large-scale in-the-wild robot manipulation dataset that reflects this trend (Khazatsky et al., 2024). By combining trajectories from different embodiments, tasks, and environments, Open X-Embodiment and similar robot-learning datasets continue this trend. On the other hand, generalist policies like Octo emphasise the increasing use of big recorded trajectory corpora for manipulation research (Ghosh et al., 2024; O'Neill et al., 2024; Walke et al., 2023). While these datasets open up new possibilities for diagnostics at the trajectory level, they also reveal a methodological flaw: angular wrap effects, which can inflate smoothness and Euclidean path length measurements, can be present in recorded motor-state signals or signals from joints. Within this framework, the DROID-100 analysis is situated in the current study. The proposed trigonometric geometry aims to prevent periodic-coordinate artefacts; however, it does not validate online safety filtering, collision avoidance, joint-limit protection, singularity avoidance, or recorded robot trajectories.

1.1. Research Gap, Aim, and Scope

The design and evaluation of robotic motion have been greatly enhanced by recent advancements in safety filters, distance-field representations, manipulator constraint handling, and large-scale robot datasets. The lack of preparation or safeguards is not the remaining void. Instead, current methods seldom combine divergent safety-margin barriers for obstacle-clearance, joint-limit, and Jacobian-singularity borders with trigonometric functions as a single planning geometry for periodic configuration spaces.

Because of this, topology-aware planning functionals that address angular branch-cut distortion and safety-margin penalisation are typically treated as independent implementation concerns.
To fill that void, this study develops a trigonometric barrier geometry for regular configuration spaces that safety-margin robots can use for motion planning. An ideal planning functional for controlled ablation and recorded-trajectory diagnostics would be one that is quotient-consistent under angular representative changes, smooth inside the safe region, and divergent at unsafe boundaries. A real-time safety-filter pathway for local command correction, torus-consistent trajectory smoothness, finite candidate search, edge-sampled admissibility checks, tangent-barrier safety margins, and sine-cosine angular embedding are all part of the architecture.
On purpose, it has limited the scope. Examining the feasibility of wrap-around continuity, singularity-margin preservation, joint-limit, and ablation behaviour under geometrically specified conditions is done through controlled simulations. In order to detect periodic-coordinate branch-cut distortion in recorded manipulation trajectories, the DROID-100 analysis is only employed as an offline real-data diagnostic. The study did not assert any validated safety at the scene level, compliance at the hardware level, manufacturer-approved validation of joint limits, or certification for real-time deployment. It adds a mathematically consistent diagnostic and planning layer that tests periodic-coordinate correction on recorded robot trajectory data and evaluates safety-margin behaviour under controlled settings.

1.2. Novelty and Contributions

The particular contribution of this study is to reframe trigonometric functions from discrete terms in forward kinematics to a topology-aware planning geometry for periodic robotic configuration spaces. The architecture integrates divergent safety-margin barriers and periodic-coordinate correction into a single planning functional. Four distinct contributions are made by the paper.

i. A torus-consistent distance and a sine-cosine angular embedding for periodic robotic configuration spaces are introduced in the paper. This depiction gives a quotient-consistent measurement of angular motion and eliminates the artificial branch-cut discontinuities that are caused by Euclidean angular subtraction.
ii. For the obstacle-clearance, joint-limit, and Jacobian-singularity margins, the tangent-barrier terms are defined in the study. Without changing the underlying periodic geometry, these barriers provide boundary-sensitive penalisation by remaining smooth inside the permissible region and diverging as a trajectory approaches risky bounds.
iii. Safety margins for tangent barriers, torus-consistent trajectory smoothness, and terminal target attraction are all part of the suggested functional. The quotient consistency, boundary divergence, interior smoothness, finite-cost nodal safety, and perturbation stability away from dangerous boundaries are the main structural qualities that it exhibits. Implementing the same geometry is done by finite candidate search, edge-sampled admissibility checks, and shortest-arc interpolation.
iv. Period-geometry correction and safety-margin penalisation are separated responsibilities in the validation. Under controlled conditions, ablation can be used to compare plans that rely just on geometry, geometry plus trigonometry, geometry plus barrier, and full geometry plus barrier. The DROID-100 diagnostic test checks if the trigonometric representation eliminates the branch-cut artefact and if the recorded periodic-coordinate motion in actual robot trajectories is inflated by the use of Euclidean angular subtraction.

2. Methodology

2.1. Problem Statement and Mathematical Setting

Consider an n-degree-of-freedom robotic manipulator with configuration $q = (q_1, \dots, q_n)$. Let $\mathcal{N} = \{1, \dots, n\}$, let $\mathcal{A} \subseteq \{1, \dots, n\}$ denote index set of periodic angular coordinates, and let $\mathcal{L} \subseteq \{1, \dots, n\}$ denote the index of mechanically limited coordinates. The two sets may overlap: a revolute joint is angular, but it may also be manufacturer-specified mechanical stops. The ambient periodic

$$\mathcal{Q}_0 = \prod_{j\in\mathcal{A}} \mathbb{T} \times \prod_{j\notin\mathcal{A}} \mathbb{R}, \qquad \mathbb{T} = R/2\pi\mathbb{Z}. \tag{1}$$

Mechanical joint limits are not removed from the topology. They are imposed as safety constraints through barrier terms. This distinction allows the formulation to preserve the periodic nature of revolute coordinates while still penalizing approach to manufacturer-specified joint-limit boundaries.

Let $\pi: \mathbb{R}^n \to \mathcal{Q}_0$ denote the quotient projection. If $k \in \mathbb{Z}^{|\mathcal{A}|}$, then q_A and $q_A + 2\pi k$ represent the same physical angular state. A planning cost J is geometrically well-defined on $\mathcal{Q}_0$ only if it is invariant under angular representative changes:

$$J(q_A, q_{\mathcal{N}\setminus\mathcal{A}}) = J(q_A + 2\pi k, q_{\mathcal{N}\setminus\mathcal{A}}), \qquad k \in \mathbb{Z}^{|\mathcal{A}|}. \tag{2}$$

The integer shifts in Eq. (2) act only on angular coordinates. This condition is the quotient-consistency requirement.

Let $\mathcal{O}_1, \ldots, \mathcal{O}_K \subseteq \mathbb{R}^3$ denote the workplace obstacle, and set let $B(q) \subset \mathbb{R}^3$ denote the robot body volume at configuration q. The clearance from obstacle $\mathcal{O}_K$ is

$$d_k(q) = \inf_{x\in B(q), y\in\mathcal{O}_k} \|x - y\|_2, \qquad d_{\text{obs}}(q) = \min_{1\le k\le K} d_k(q). \tag{3}$$

A clearance tolerance $d^\star > 0$ is imposed, so collision safety requires $d_{\text{obs}}(q) > d^\star$.

Let $T_e(q) \in SE(3)$ denote the end-effector pose, and let $J_x(q) \in \mathbb{R}^{m\times n}$, $m \le 6$, denote the corresponding task Jacobian. The Jacobian singularity margin is

$$s(q) = \sigma_{\min}(J_x(q)), \tag{4}$$

where $\sigma_{\min}$denotes the smallest singular value. A singularity tolerance $\sigma^\star > 0$ is imposed, so singularity safety requires $s(q) > \sigma^\star$.

For each mechanically limited coordinate $j \in \mathcal{L}$, let $q_j^- < q_j^+$ enote the admissible joint interval in the selected manufacturer-specified chart. For angular joints with mechanical stops, this interval is understood in the corresponding manufacturer-specified angular branch. Define the normalized joint-limit margin by

$$m_{\text{lim}}(q) = \min_{j\in\mathcal{L}} \left[\frac{2\min\{q_j - q_j^-, q_j^+ - q_j\}}{q_j^+ - q_j^-}\right], \tag{5}$$

with $m_{\text{lim}}(q) = 1$ if $\mathcal{L} = \emptyset$. Thus, $m_{\text{lim}}(q) > 0$ means that every mechanically limited coordinate lies strictly inside its admissible interval.

The safe planning set is

$$\mathcal{S} = \{q \in \mathcal{Q}_0 : d_{\text{obs}}(q) > d^\star, \qquad m_{\text{lim}}(q) > 0, \qquad s(q) > \sigma^\star\}. \tag{6}$$

Thus, $\mathcal{S}$ excludes collision-risk states, joint-limit boundary states, and near-singular configurations.

Definition 1 (Admissible Trajectory): For horizon $H \in \mathbb{N}$, a trajectory $q_{0:H} = (q_0, \ldots, q_H)$ is admissible if q_0 is fixed, $q_H \in \mathcal{G} \subset \mathcal{S}$, and $q_t \in \mathcal{S}$ for all $t = 0, \ldots, H$. The admissible trajectory class is

$$\Gamma_H(q_0, \mathcal{G}) = \{q_{0:H} : q_0 \text{ is fixed}, \ q_H \in \mathcal{G}, \ q_t \in \mathcal{S}\ \forall t = 0, \ldots, H\}. \tag{7}$$

The Euclidean increment $\|\tilde{q}_{t+1} - \tilde{q}_t\|_2^2$ is not intrinsic on $\mathcal{Q}_0$ when angular coordinates are present.

Proposition 1 (Euclidean Angular Subtraction is not Quotient-Consistent): Let $\theta, \phi \in \mathbb{T}$, and let $\tilde{\theta}, \tilde{\phi} \in \mathbb{R}$ be representatives. The expression $|\tilde{\theta} - \tilde{\phi}|$ does not define an intrinsic distance on $\mathbb{T}$.

Proof. Take $\tilde{\theta} = \pi - \varepsilon$ and $\tilde{\phi} = -\pi + \varepsilon$, where $0 < \varepsilon \ll 1$. On $\mathbb{T}$, the two points are separated by the short periodic arc of length 2ε. Direct Euclidean subtraction gives

$$|\tilde{\theta} - \tilde{\phi}| = 2\pi - 2\varepsilon.$$

As $\varepsilon \downarrow 0$, the physical periodic separation tends to 0, whereas the Euclidean coordinate difference tends to 2π. Hence Euclidean subtraction depends on the chosen lift and violates Eq. (2). ■

The planning problem is to construct a functional that is quotient-consistent on angular coordinates and divergent at the unsafe boundary of $\mathcal{S}$.

Problem 1 (Trigonometric Barrier Motion Planning): Given $q_0 \in \mathcal{S}$, a goal set $\mathcal{G} \subset \mathcal{S}$, obstacles $\mathcal{O}_1, \ldots, \mathcal{O}_K$, joint limits $\{q_j^-, q_j^+\}_{j\in\mathcal{L}}$, clearance tolerance $d^\star > 0$, and singularity tolerance $\sigma^\star > 0$, find

$$q_{0:H}^\star \in \arg\min_{q_{0:H}\in\Gamma_H(q_0,\mathcal{G})} \mathcal{J}_H(q_0{:}H), \tag{8}$$

where $\mathcal{J}_H$is quotient-consistent, smooth in the interior of $\mathcal{S}$, and divergent as trajectory node approaches $d_{\text{obs}} = d^\star$, $m_{\text{lim}} = 0$, or $s = \sigma^\star$.
Central constraints in manipulator motion planning and safe human-robot interaction include preserving obstacle clearance, avoiding joint limits, handling redundancy, and being aware of singularities (Aydogmus & Boztas, 2024; Baron et al., 2020; Li et al., 2023; Secil & Ozkan, 2023; Zhang et al., 2025a).
The principal notation used in the mathematical formulation is summarized in Table 1

Table 1. Core notation used in the trigonometric planning formulation.

Symbol	Meaning
$\boldsymbol{q = (q_1, \dots, q_n)}$	Robot configuration
$\boldsymbol{\mathcal{N} = \{1, \dots, n\}}$	Full coordinate index set
$\boldsymbol{\mathcal{A} \subseteq \mathcal{N}}$	Index set of periodic angular coordinates
$\boldsymbol{\mathcal{L} \subseteq \mathcal{N}}$	Index set of mechanically limited coordinates
$\mathbb{T} = \mathbb{R}/\boldsymbol{2\pi\mathbb{Z}}$	Periodic angular coordinate space
$\boldsymbol{\mathcal{Q}_0}$	Ambient periodic configuration space
$\boldsymbol{\pi}: \mathbb{R}^{\boldsymbol{n}} \to \boldsymbol{\mathcal{Q}_0}$	Quotient projection from lifted coordinates to physical configurations
$\boldsymbol{\mathcal{B}(q)}$	Robot body volume at configuration q
$\boldsymbol{\mathcal{O}_k}$	k-th workspace obstacle
$\boldsymbol{d_k(q)}$	Clearance from obstacle $\mathcal{O}_k$
$\boldsymbol{d_{\text{obs}}(q)}$	Minimum obstacle clearance
$\boldsymbol{T_e(q)}$	End-effector pose
$\boldsymbol{J_x(q)}$	Manipulator task Jacobian
$\boldsymbol{s(q) = \sigma_{\min}(J_x(q))}$	Jacobian singularity margin
$\boldsymbol{m_{lim}(q)}$	Normalized joint-limit margin
$\boldsymbol{\mathcal{S}}$	Safe planning set
$\boldsymbol{\mathcal{G}}$	Goal region
$\boldsymbol{q_{0:H} = (q_0, \dots, q_H)}$	Discrete trajectory over horizon H
$\boldsymbol{\Gamma_H(q_0, \mathcal{G})}$	Admissible trajectory class from q_0 to $\mathcal{G}$
$\boldsymbol{\mathcal{J}_H}$	Trigonometric planning functional

2.2. Trigonometric Configuration Embedding

Define the angular embedding $\varphi: \mathbb{T} \to \mathbb{R}^2$ by $\varphi(\theta) = (\cos\theta, \sin\theta)$. For a lifted representative $q \in \mathbb{R}^2$ of a physical configuration in $\mathcal{Q}_0$, define the full trigonometric embedding by

$$\Phi(q) = \left(\left(\cos q_j, \sin q_j\right)_{j\in\mathcal{A}}, \left(q_j\right)_{j\notin\mathcal{A}}\right) \in \mathbb{R}^{2|\mathcal{A}|+|\mathcal{N}\setminus\mathcal{A}|}. \tag{9}$$

Proposition 2 (Periodic Invariance of Trigonometric Embedding): For every angular integer shift $k \in \mathbb{Z}^{|\mathcal{A}|}$, $\Phi\left(q_{\mathcal{A}} + 2\pi k, q_{\mathcal{N}\setminus\mathcal{A}}\right) = \Phi\left(q_{\mathcal{A}} + q_{\mathcal{N}\setminus\mathcal{A}}\right)$.
Proof. For each $j \in \mathcal{A}$, the trigonometric identities $\cos\left(q_j + 2\pi k_j\right) = \cos q_j$ and $\sin\left(q_j + 2\pi k_j\right) = \sin q_j$ hold for every $k_j \in \mathbb{Z}$. The non-angular coordinates $q_j, j \notin \mathcal{A}$, are unchanged. Therefore, the full embedding is invariant under angular representative changes. ■
Eq. (9) removes the artificial branch cut from periodic coordinates by representing each angular coordinate through its sine-cosine image rather than through a selected real-valued angular branch.

2.3. Torus-Consistent Distance and Smoothness

For two physical configurations $q, p \in \mathcal{Q}_0$, choose any lifted representative in $\mathbb{R}^n$. Define the weighted trigonometric squared distance by

$$d^2_{\text{trig}}(q,p) = \sum_{j\in\mathcal{A}} \omega_j\{2 - 2\cos\left(q_j - p_j\right)\} + \sum_{j\notin\mathcal{A}} \omega_j\left(q_j - p_j\right)^2, \qquad \omega_j > 0. \tag{10}$$

The value of Eq. (10) does not depend on the selected angular representative because angular part is invariant under 2π-shifts. For angular coordinates, $2 - 2\cos(q_j - p_j)$ is the squared chordal distance on the unit circle. Thus, Eq. (10) is quotient-consistent and locally agrees with squared Euclidean angular displacement for small angular increments.

Proposition 3 (Local Euclidean Agreement): For $|\delta| \ll 1$,

$$2 - 2\cos\delta = \delta^2 + O(\delta^4).$$

Proof. The Taylor expansion $\cos\delta = 1 - \delta^2/2 + O(\delta^4)$ gives
$2 - 2\cos\delta = 2 - 2\left(1 - \delta^2/2 + O(\delta^4)\right) = \delta^2 - O(\delta^4)$. Hence the angular chordal term agrees with squared Euclidean angular displacement to second order. ■

Proposition 4 (Embedded-Distance Equivalence): For $j \in \mathcal{A}$,

$$\left\|\varphi(q_j) - \varphi(p_j)\right\|_2^2 = 2 - 2\cos(q_j - p_j).$$

Proof. Using $\varphi(\theta) = (\cos\theta, \sin\theta)$, we obtain

$$\left\|\varphi(q_j) - \varphi(p_j)\right\|_2^2 = \left(\cos q_j - \cos p_j\right)^2 + \left(\sin q_j - \sin p_j\right)^2$$

Expanding the right-hand side and simplification gives

$$\left\|\varphi(q_j) - \varphi(p_j)\right\|_2^2 = 2 - 2\cos(q_j - p_j)$$

this proves the identity. ■

The first-order trajectory smoothness functional is

$$R_H(q_{0:H}) = \sum_{t=0}^{H-1} d_{\text{trig}}^2(q_{t+1}, q_t). \tag{11}$$

This functional replaces Euclidean joint-space smoothing with torus-consistent smoothing. It therefore avoids artificial smoothness penalties caused by angular branch-cut crossings.

2.4. Tangent Barriers for Unsafe Boundaries

For a safety margin μ and scale $r > 0$, define the extended tangent barrier by

$$\psi_r(\mu) = \begin{cases} \tan^2\left(\frac{\pi}{2}\frac{r}{\mu + r}\right), & \mu > 0, \\ +\infty, & \mu \le 0 \end{cases} \tag{12}$$

The map $\psi_r$is smooth on $(0, \infty)$, nonnegative, and divergent as $\mu \downarrow 0$. Thus, a finite barrier value is possible only when the corresponding safety margin is strictly positive.

For obstacle $\mathcal{O}_k$, define the obstacle safety margin by $\mu_k^{\text{obs}}(q) = d_k(q) - d_k^\star$, where $d_k^\star > 0$. The obstacle barrier is

$$B_{\text{obs}}(q) = \sum_{k=1}^{K} \beta_k \psi_{r_k^{\text{obs}}}\left(\mu_k^{\text{obs}}(q)\right), \qquad \beta_k > 0. \tag{13}$$

For each mechanically limited coordinate $j \in \mathcal{L}$, define the lower and upper joint limit margins by

$$\mu_j^-(q) = q_j - q_j^-, \qquad \mu_j^+(q) = q_j^+ - q_j.$$

The joint-limit barrier is

$$B_{\text{lim}}(q) = \sum_{j \in \mathcal{L}} \alpha_j \left[\psi_{r_j^-}\left(\mu_j^-(q)\right) + \psi_{r_j^+}\left(\mu_j^+(q)\right)\right], \qquad \alpha_j > 0. \tag{14}$$

For singularity avoidance, define singularity safety margin by $\mu^{\text{sing}}(q) = s(q) - \sigma^\star$. The singularity barrier is

$$B_{\text{sing}}(q) = \gamma\psi_{r_s}\left(\mu^{\text{sing}}(q)\right), \qquad \gamma > 0. \tag{15}$$

The total barrier is

$$B(q) = B_{\text{obs}}(q) + B_{\text{lim}}(q) + B_{\text{sing}}(q). \tag{16}$$

Barrier and safety-filter formulations are widely used in safety-critical control to encode boundary-sensitive constraints. The present formulation differs by defining the barrier on a trigonometric planning geometry for periodic robotic configurations, so that safety-margin penalization is combined with quotient-consistent angular motion (Cohen et al., 2024; Garg et al., 2024; Hsu et al., 2024).

2.5. Unified Trigonometric Planning Functional

For a goal configuration $q_g \in \mathcal{G}$, define the trigonometric planning function by

$$\mathcal{J}_H(q_0{:}H) = \lambda_g d^2_{\text{trig}}(q_H, q_g) + \lambda_s R_H(q_{0:H}) + \lambda_b \sum_{t=0}^{H} B(q_t), \qquad \lambda_g, \lambda_s, \lambda_b > 0. \tag{17}$$

For a goal region, the terminal attraction term may be replaced by

$$\lambda_g \inf_{g \in \mathcal{G}} d^2_{\text{trig}}(q_H, g).$$

Eq. (17) is the explicit objective used in Eq. (8). It combines terminal goal attraction, torus-consistent trajectory smoothness, and divergent tangent barriers for unsafe boundaries.

The objective in Eq. (17) separates two mechanisms that are evaluated in the ablation study. The trigonometric distance terms define quotient-consistent motion geometry on the periodic configuration space, whereas the tangent-barrier terms impose boundary-sensitive penalties through obstacle-clearance, joint-limit, and singularity margins. Therefore, the trigonometric-only planner isolates the effect of periodic geometry, the barrier-only planner isolates the effect of safety-margin penalization, and the full trigonometric-barrier planner evaluates their coupled contribution.

2.6. Mathematical Properties

Theorem 1 (Quotient Consistency of $\mathcal{J}_{\mathcal{H}}$): The functional in Eq. (17) is invariant under 2π-shifts of angular coordinates.

Proof. The terminal goal term and the smoothness term depend on angular coordinates only through cosine differences. These quantities are invariant under angular representative changes. The robot body volume, obstacle distances, task Jacobian, and singularity margin are functions of the physical configuration, not of a particular lifted angular representative. The tangent-barrier terms therefore also remain unchanged under 2π-shifts of angular coordinates. Hence all terms in Eq. (17) satisfy the quotient-consistency requirement in Eq. (2). ■

Theorem 2 (Boundary Divergence): If any trajectory node approaches an obstacle boundary $\mu_k^{\text{obs}} \downarrow 0$, a joint-limit boundary $\mu_j^-(q_t) \downarrow 0$ or $\mu_j^+(q_t) \downarrow 0$, or a singularity boundary $\mu^{\text{sing}}(q_t) \downarrow 0$, then $B(q_t) \to \infty$.

Proof. For every margin $\mu > 0$, and scale $r > 0, r/(\mu + r) \uparrow 1$ as $\mu \downarrow 0$. Hence $\frac{\pi}{2}\frac{r}{\mu+r} \uparrow \frac{\pi}{2}$, and therefore, $\tan^2\left(\frac{\pi}{2}\frac{r}{\mu+r}\right) \to \infty$.

Since each obstacle, joint-limit, and singularity barrier is a positive multiple of this expression, the corresponding barrier term diverges. Thus $B(q_t) \to \infty$.■

Corollary 1 (Finite-Cost Nodal Safety): If $\mathcal{J}_H(q_0{:}H) < \infty$, then every evaluated node q_t lies in $\mathcal{S}$.

Proof. If some evaluated node $q_t \notin \mathcal{S}$, then at least one safety margin is nonpositive: an obstacle margin, a joint-limit margin, or the singularity margin. By Eq. (12), the corresponding tangent barrier is $+\infty$. Since Eq. (17) sum the barrier values over all trajectory node with $\lambda_b > 0$, this would imply $\mathcal{J}_H(q_0{:}H) = \infty$, contradicting finite-cost assumption. Therefore, every evaluated node satisfies $q_t \notin \mathcal{S}$. ■

Proposition 5 (Interior Smoothness): Assume that the obstacle-clearance functions $d_k(q)$, the task Jacobian $J_x(q)$, and the singularity margin $s(q)$ are continuously differentiable on a compact subset $K \subset \mathcal{S}$, away from non-smooth obstacle-distance points and singularity-value multiplicities. Then $B(q)$ and $\mathcal{J}_{\mathcal{H}}$ are continuously differentiable on K.

Proof. On $K \subset \mathcal{S}$ is compact, all obstacle, joint-limit, and singularity margins have positive lower bounds on K. Therefore, the arguments of the tangent barrier remain inside $(0, \pi/2)$. The maps

$$\mu \mapsto \frac{r}{(\mu + r)}, \qquad x \mapsto \tan^2\left(\frac{\pi x}{2}\right), (p, q) \mapsto d^2_{\text{trig}}(q, p)$$

are smooth on their respective domains. By composition with differentiable margin functions, $B(q)$ is continuously differentiable on K. The functional $\mathcal{J}_H$ is a finite sum of continuously differentiable terminal, smoothness, and barrier terms, so it is continuously differentiable on K. ■

Proposition 6 (Perturbation Stability away from Boundary): Let $K \subset \mathcal{S}$ be compact, and assume that all obstacle, joint-limit, and singularity margins on K are bounded below by some $\delta > 0$. Then there exists as constant $L_K > 0$ such that, for any two trajectories $q_{0:H}, p_{0:H} \subset K$,

$$|\mathcal{J}_H(q_0{:}H) - \mathcal{J}_H(p_0{:}H)| \leq L_K \sum_{t=0}^{H} \|\Phi(q_t) - \Phi(p_t)\|_2. \tag{18}$$

Proof. On K, all safety margins are bounded away from zero. Hence the tangent-barrier arguments remain below $\pi/2$ by a positive margin, and all derivatives of the barrier terms are bounded. The terminal and smoothness terms are also smooth functions of the embedded trigonometric representation. Therefore, the gradient of $\mathcal{J}_H$ is bounded on the compact set of trajectories with nodes in K. Applying the mean-value theorem term by term gives the stated Lipschitz-type perturbation bound. ■

Corollary 1 guarantees safety only at the evaluated trajectory nodes. It does not certify continuous-edge safety between consecutive nodes. Certified segment collision checking, dense resampling, or interpolation-based admissibility checks are therefore still required for continuous-motion safety. The simulation procedure below includes this additional edge-checking criterion.

2.7. Real-Time Trigonometric Safety Filter

Let $u_t^0 \in \mathbb{R}^m$ denote a nominal control command at time t, and let $F_h(q_t, u)$ denote a discrete-time local motion model over one sampling interval $h > 0$. Safety-filter architectures provide a supervisory layer between nominal control and constraint enforcement in safety-critical systems (Ames et al., 2017; Hsu et al., 2024; Wabersich & Zeilinger, 2021).

Let $\mathbb{U}(q_t) \subset \mathbb{R}^m$ denote the admissible action set, including actuator, velocity, and task-dependent command limits. The trigonometric safety filter modifies u_t^0 only when the predicted state approaches the unsafe boundary. It is defined by

$$u_t^\star \in \arg\min_{u \in \mathbb{U}(q_t)} \left\{ \|u - u_t^0\|_R^2 + \eta B\big(F_h(q_t, u)\big) \right\}, \tag{19}$$

where

$$\|v\|_R^2 = v^\top R v, \;\; R \succ 0, \;\; \eta > 0$$

and B is the aggregate tangent-barrier functional defines in Eq. (16). Since $B(q) = +\infty$ for $q \notin \mathcal{S}$, for $q \notin$, any finite-cost solution of Eq. (19) satisfies $F_h(q_t, u_t^\star) \in \mathcal{S}$.

Thus, the filter preserves the nominal command when the predicted state remains admissible and applies the smallest R-weighted correction needed to keep the one-step predicted state inside the safe planning set. In implementation, the infinite barrier is enforced through explicit feasibility checks on $F_h(q_t, u)$, while large finite barrier values are used only for numerical conditioning. If no feasible finite-cost action exists, the controller stops, replans, or activates a fail-safe mode.

The filter is treated as an online extension of the trigonometric barrier geometry. Its safety-margin behavior is evaluated in controlled simulation. The DROID-100 analysis is used only for offline periodic-coordinate diagnostics and is not used to certify real-time safety-filter performance.

2.8. Algorithmic Implementation and Optimization Procedure

Let $Q = (q_0, \ldots, q_H)$ be a discrete trajectory with fixed initial configuration q_0. The terminal configuration is handled through the goal term in Eq. (17), or through a hard terminal constraint when $q_H \in \mathcal{G}$ is prescribed. Accordingly, the free optimization nodes are denoted by

$$Q_{\text{free}} = (q_1, \ldots, q_{H-1}),$$

with q_H removed Q_{free} when the terminal configuration is fixed. Angular coordinates are updated in a lifted chart, while distances and costs are evaluated through the quotient-consistent quantities in Eqs. (10) and (17).

Given an iterate $Q^{(\ell)}$, a generic descent update can be written as

$$Q_{\text{free}}^{(\ell+1)} = \mathcal{W}\left[Q_{free}^{(\ell)} - \alpha_\ell M_\ell^{-1} \nabla_{Q_{free}} \mathcal{J}_{\mathcal{H}}\left(Q^{(\ell)}\right)\right], \tag{20}$$

where $\alpha_\ell > 0$, $M_\ell \succ 0$, and $\mathcal{W}$ maps angular components back to the chosen lifted representatives without changing the corresponding element of $\mathbb{T}$. A candidate update is accepted only if

$$\mathcal{J}_H\left(Q^{(\ell+1)}\right) < \mathcal{J}_H\left(Q^{(\ell)}\right), \qquad \mathcal{J}_H\left(Q^{(\ell+1)}\right) < \infty.$$

Since Corollary 1 ensures safety only at evaluated trajectory nodes, every edge is also checked by interpolation. For $t = 0, \dots, H-1$, let

$$\mathcal{E}_\Delta(q_t, q_{t+1}) = \{z_{t,r} : r = 0, \dots, N_\Delta\}$$

be the set of interpolated samples between q_t and q_{t+1}. Angular coordinates follow the shortest arc on $\mathbb{T}$, while non-angular coordinates are interpolated linearly. The edge-safety condition is

$$z \in \mathcal{S} \qquad \forall z \in \mathcal{E}_\Delta(q_t, q_t + 1), \qquad t = 0, \dots, (H-1). \tag{21}$$

A trajectory is accepted only if it has finite cost, decreases the objective, and satisfies the edge-sample admissibility condition in Eq. (21).

For controlled simulation, Eq. (20) is implemented through a deterministic finite candidate search rather than through high-dimensional gradient optimization. A finite candidate set

$$\mathcal{C} = \left\{Q^{(1)}, \dots, Q^{(N_c)}\right\}$$

is generated from shortest-arc interpolation, barrier-biased perturbations, and ablation-specific variants. The selected trajectory is

$$Q^\star \in \arg\min_{Q \in \mathcal{C}_{\text{adm}}} \mathcal{J}_{\mathcal{H}}(Q), \tag{22}$$

where

$$\mathcal{C}_{\text{adm}} = \{Q \in C : q_t \in \mathcal{S}\ \forall t, and\ Eq.(21)\ holds\ for\ every\ edge\}.$$

If $\mathcal{C}_{\text{adm}} = \emptyset$, the planner returns failure. In the controlled validation, this finite-search method avoids unstable high-dimensional numerical optimisation while preserving the mathematical structure of Eq. (8).

Algorithm 1. Trigonometric Barrier Trajectory Optimization

Input: $q_0, \mathcal{G}, H, \mathcal{O}, d^\star, \sigma^\star, \lambda_g, \lambda_s, \lambda_b$.

Output: $Q^\star = q_{0:H}^\star$ or failure.

i. Generate candidate trajectories $\mathcal{C}$ using shortest-arc angular interpolation and control-point perturbations.
ii. For each $Q \in \mathcal{C}$, compute $R_H(Q)$, B_{obs}, B_{lim}, B_{sing}, and $\mathcal{J}_H(Q)$.
iii. Reject Q if $\mathcal{J}_H(Q) = \infty$.
iv. Reject Q if any interpolated edge violates Eq. (21).
v. Select the finite-cost trajectory with minimum $\mathcal{J}_H$.
vi. Return $Q^\star$, or failure if no admissible candidate exists.

The proposed trigonometric planning geometry is implemented in Algorithm 1 using a finite candidate-search variant. The torus-consistent distance identifies smoothness without wrap-around artefacts, the sine-cosine representation maintains angular periodicity, and the tangent barriers impose safety limits by means of boundary-sensitive penalties. With the use of the edge-sampling condition in Eq. (21) we may verify admissibility along interpolated motion segments as well as at discrete trajectory nodes.

2.9. Controlled Simulation Design

Let $\mathcal{M} = \{\mathcal{M}_1, \mathcal{M}_2, \mathcal{M}_3, \mathcal{M}_4\}$ denote the planner set, where

$\mathcal{M}_1 =$ Euclidean, $\mathcal{M}_2 =$ Trig-only, $\mathcal{M}_3 =$ Barrier-only, $\mathcal{M}_4 =$ Full trig-barrier.

Below is a summary of the versions, which differ solely in terms of smoothness and safety. the controlled simulation makes use of planner-variant structures.

Planner	Smoothness term	Safety term

$\mathcal{M}_1$	$\|q_{t+1} - q_t\|_2^2$	finite diagnostic penalty
$\mathcal{M}_2$	$d_{\text{trig}}^2(q_{t+1} - q_t)$	finite diagnostic penalty
$\mathcal{M}_3$	$\|q_{t+1} - q_t\|_2^2$	$B(q)$
$\mathcal{M}_4$	$d_{\text{trig}}^2\|q_{t+1} - q_t\|_2^2$	$B(q)$

The primary validation set is

$$\mathcal{V}_{\text{main}} = \{\text{angular wrap, joint-limit grazing, near-singular reach, combined}\}$$

The supplementary diagnostic set is

$$\mathcal{V}_{\text{diag}} = \{\text{obstacle clutter, narrow passage, perturbed tracking}\}$$

Only $\mathcal{V}_{\text{main}}$ is used for the main quantitative claims. The supplementary diagnostic scenarios are retained only to examine qualitative stress behavior under obstacle clutter, narrow passages, and tracking perturbations. For each planner $\mathcal{M}_i$ and scenario v, the trajectory $q_{0:H}^{(i,v)}$ is summarized by

$$\mathcal{D}(q_{0:H}) = \left(\text{Succ}, \min_{0\le t\le H} s\,(q_t), \min_{0\le t\le H} m_{\text{lim}}\,(q_t), E_{\text{wrap}}, R_H(q_{0:H})\right). \tag{23}$$

Here Succ $\in \{0,1\}$. The angular wrap excess E_{wrap} measures the excess path length produced by raw Euclidean angular subtraction relative to the shortest periodic angular displacement. It is defined by

$$E_{\text{wrap}}(q_{0:H}) = \sum_{t=0}^{H-1}\sum_{j\in\mathcal{A}}\left[\left|q_{t+1,j} - q_{t,j}\right| - \left|\operatorname{atan2}\left(\sin\left(q_{t+1,j} - q_{t,j}\right), \cos\left(q_{t+1,j} - q_{t,j}\right)\right)\right|\right]_+,$$

$\max\{x, 0\}$. This diagnostic is zero when the Euclidean angular increment agrees with the shortest periodic increment.

A trajectory is classified as successful when

$$q_H \in \mathcal{G}, \qquad q_t \in \mathcal{S}\ \forall t = 0, \dots H, \qquad z \in \mathcal{S}\ \forall z \in \mathcal{E}_{\Delta}(q_t, q_{t+1}),\ t = 0, \dots, (H-1). \tag{24}$$

The simulation evaluates three properties:

Periodic correction: $E_{\text{wrap}}(\mathcal{M}_4) \le E_{wrap}(\mathcal{M}_1)$,

Safety-margin preservation: $\min_{0\le t\le H} s\,(q_t) > 0, \min_{0\le t\le H} m_{\text{lim}}\,(q_t) > 0$,

ablation effect: $\mathcal{M}_2$ isolates d_{trig}, $\mathcal{M}_3$ isolates B, $\mathcal{M}_4$ combines both mechanisms.

Thus, the controlled simulation is restricted to wrap-around continuity, singularity-margin preservation, joint-limit margin preservation, and ablation behaviour. Obstacle-clutter, narrow-passage, and perturbed-tracking cases are retained only as supplementary diagnostics and are not used as primary basis for the main quantitative claims.

2.10. Real-Data Application Protocol

The real-data layer uses the public DROID-100 subset as an offline recorded-trajectory diagnostic for periodic-coordinate effects in robot motor-state data. DROID contains large-scale in-the-wild manipulation demonstrations, which makes it suitable for testing whether angular branch cuts affect recorded robot trajectories (Khazatsky et al., 2024). The analysis is restricted to periodic-coordinate diagnostics; it does not certify collision avoidance, manufacturer joint-limit safety, Jacobian singularity avoidance, or real-time safety-filter performance.

Let $q_{1:M} = (q_1, \dots, q_M)$ be a recorded motor-state trajectory, and let $\mathcal{A}_{\mathcal{D}}$ denote the motor-state channels treated as periodic in the diagnostic analysis. These channels are used only for periodic-coordinate path diagnostics. They are not treated as a calibrated manufacturer-certified joint model.

The Euclidean periodic-coordinate path length is

$$L_{\text{Euc}}(q_{1:M}) = \sum_{t=1}^{M-1}\left(\sum_{j\in\mathcal{A}_{\mathcal{D}}}\left(q_{t+1,j} - q_{t,j}\right)^2\right)^{1/2}. \tag{25}$$

The trigonometric shortest-periodic path length is

$$L_{\text{trig}}(q_{1:M}) = \sum_{t=1}^{M-1} \left(\sum_{j \in \mathcal{A}_{\mathcal{D}}} \delta_{\mathbb{T}} \left(q_{t+1,j}, q_{t,j} \right)^2 \right)^{1/2}, \tag{26}$$

where

$$\delta_{\mathbb{T}}(a, b) = \operatorname{atan2}\big(sin(a-b), cos(a-b)\big) \epsilon (-\pi, \pi]$$

is the signed shortest periodic angular displacement from bbb to aaa. The angular wrap excess is

$$E_{\text{wrap}}(q_{1:M}) = L_{\text{Euc}}(q_{1:M}) - L_{\text{trig}}(q_{1:M}). \tag{27}$$

A local wrap event is recorded when

$$\left| q_{t+1,j} - q_{t,j} \right| > \pi, \qquad j \in \mathcal{A}_{\mathcal{D}}. \tag{28}$$

The sine-cosine embedding is evaluated through the numerical unit-circle identity error

$$\varepsilon_{\text{unit}} = \max_{1 \le t < M, j \in \mathcal{A}_{\mathcal{D}}} \left| \sin^2\left(q_{t,j}\right) + \cos^2\left(q_{t,j}\right) - 1 \right|, \tag{29}$$

and the chordal-distance identity error

$$\varepsilon_{\text{chord}} = \max_{1 \le t < M, j \in \mathcal{A}_{\mathcal{D}}} \left| \left\| \varphi\left(q_{t+1,j}\right) - \varphi\left(q_{t,j}\right) \right\|_2^2 - \left\{ 2 - 2\cos\left(\delta_{\mathbb{T}}\left(q_{t+1,j}, q_{t,j}\right) \right) \right\} \right|. \tag{30}$$

The DROID-100 analysis therefore tests whether recorded robot trajectories contain angular branch-cut artefacts and whether the proposed trigonometric representation removes the resulting Euclidean path inflation. Safety-margin claims involving $B_{\text{lim}}, B_{\text{sing}}, s(q)$, and the online filter in Eq. (19) are evaluated only in controlled simulation, where the required geometry, Jacobian, and admissible set are explicitly defined.

The proposed workflow is summarised in Figure 1. commence with a periodic manipulator planning problem, fix angular geometry with sine-cosine embedding and torus-consistent distance, and add tangent barriers for obstacle-clearance, joint-limit, and singularity margins in the framework. The mathematical analysis of quotient consistency, boundary divergence, nodal safety, smoothness, and perturbation stability is performed on this unified planning functional. A real-time safety-filter pathway, edge-sampled admissibility tests, shortest-arc interpolation, and finite candidate search are all used in the implementation. For safety-margin and ablation behaviour, validation is divided into controlled simulation, and for periodic-coordinate wrap correction in recorded robot trajectories, DROID-100 diagnostics.



Figure 1. Methodological workflow of the proposed trigonometric barrier planning framework.

3. Simulation

3.1. Controlled Numerical Evaluation

The proposed planner is tested in the controlled numerical assessment with known safety-margin diagnostics, preset kinematic situations, and explicit admissibility constraints. Detailed start and terminal setups, as well as planner-variant definitions, are included in Appendix Table A1, and Table 2 summarises the main and supplementary simulation scenarios. The main cases study topics such as wrap-around continuity, preservation of the joint-limit margin, preservation of the Jacobian singularity-margin, and the combined impact of periodic geometry and tangent barriers. Instead of using them as the major basis for the quantitative claims, the obstacle-clutter, narrow-passage, and perturbed-tracking scenarios are kept as extra diagnostics.

A full trigonometric-barrier planner, an only-trigonometric planner, an only-barrier planner, and a Euclidean baseline planner are the four versions that are compared. The effects of tangent-barrier safety penalisation and torus-consistent distance are isolated by this ablation. These metrics are listed in Table 3: success status, minimal singularity margin $\min_t s\,(q_t)$, minimum normalised joint-limit margin $\min_t m_{\text{lim}}\,(q_t)$, angular wrap excess, and the trigonometric smoothness functional R_H.

3.2. Periodic Wrap-Around Behavior

The angular-wrap scenario isolates the discontinuity created by the $-\pi/\pi$ branch cut. Table 3 shows that the Euclidean baseline and the barrier-only planner both follow the long coordinate path, producing a wrap excess of 5.963 and (R_H = 1.039). In contrast, the trigonometric-only and full trigonometric-barrier planners reduce the wrap excess to 0.000 and R_H to 0.001.

Figure 2 shows the same effect at the trajectory level. The Euclidean representation produces an artificial long displacement when the first joint crosses the angular branch cut, whereas the trigonometric variants follow the shortest periodic arc. This result supports the main geometric claim that d_{trig} removes branch-cut artefacts while preserving the physical configuration.

3.3. Singularity and Joint-Limit Margins

The scenario that approaches the singularity tests if the tangent-barrier terms maintain a positive margin for the Jacobian singularity. Both Table 3 and Figure 3 demonstrate that when $\min_t s\,(q_t)$ = 0.000, the trigonometric-only planner and the Euclidean baseline both fails. In comparison, both the barrier-only and full trigonometric-barrier planners succeed in achieving trajectories with $\min_t s\,(q_t)$ = 0.050. This finding demonstrates that while trigonometric distance can rectify angular geometry, it is insufficient to guarantee protection from singularity margins on its own. The active mechanism that maintains distance from the singularity boundary is the tangent barrier.

A less discriminatory situation is the joint-limit grazing scenario. The minimal normalised joint-limit margin, $\min_t m_{\text{lim}}\,(q_t)$ = 0.431, is maintained by all planner variants. The positive joint-limit margin is maintained across the principal-controlled scenarios, as shown in Figure 4. This finding should be taken with a grain of salt: the full trigonometric barrier planner that has been suggested maintains joint-limit feasibility, but in this particular case, we do not see any distinct benefit above the comparator planners in terms of joint-limit.

3.4. Coupled Constrained Performance

The most robust main test is the combination scenario, which concurrently incorporates safety-margin requirements and angular wrap-around effects. Given a wrap excess of 5.883, a singularity margin of $\min_t s\,(q_t)$ = 0.004, and R_H = 1.164, the Euclidean baseline is rejected. Though it eliminates the wrap excess, the trigonometric-only planner is still inadequate due to the absence of the tangent-barrier method. Even though it also fails, the barrier-only planner manages to increase the singularity margin from 0.004 to 0.013 while keeping the 5.883-point Euclidean wrap excess.

Among all possible combinations, only the full trigonometric-barrier planner achieves success. The result is zero wrap excess, with $\min_t m_{\text{lim}}(q_t) = 0.590$, $\min_t s(q_t) = 0.087$, and $R_H = 0.465$. According to this design, the two parts serve separate purposes: d_{trig} fixes periodic-coordinate distortion, and $B(q)$ discourages movement close to potentially dangerous borders.

3.5. Ablation Evidence

In comparison to the geometric baseline, Figure 5 displays the ablation effects in all of the controlled conditions. There is no one component responsible for the observed improvements, as shown by the heatmap. The alternative that simply uses trigonometry primarily modifies periodic-motion smoothness and decreases wrap excess. Only the singularity-margin preservation is enhanced by the barrier-only form. To date, in the linked limited case, no planner has been more successful than the full trigonometric-barrier planner, which integrates both effects.

The results obtained under these controlled conditions lend credence to the postulated mechanism. Under known geometry, they show that they can correct wrap-arounds, preserve singularity margins, make joint limits feasible, and behave as ablation targets. Neither their validity at the hardware level nor their certification against real-world collisions are warranted.

Table 2. Controlled simulation matrix and planner variants.

Scenario	Role	Obstacles	Main tested property	Main-text use
Angular wrap	Primary	0	Periodic wrap-around continuity	Main result
Joint-limit grazing	Primary	0	Joint-limit margin preservation	Main result
Near-singular reach	Primary	0	Jacobian singularity avoidance	Main result
Combined	Primary	4	Coupled wrap, singularity, and barrier effects	Main result
Obstacle clutter	Stress test	3	Link-aware obstacle clearance	Supplementary diagnostic
Narrow passage	Stress test	4	Narrow-passage feasibility	Supplementary diagnostic
Perturbed tracking	Robustness	3	Post-perturbation safety margins	Supplementary diagnostic

Table 3. Quantitative performance summary for primary controlled scenarios.

Scenario	Method	Success	$\min_t s(q_t)$	$\min_t m_{\text{lim}}(q_t)$	Wrap Excess	R_H
Angular wrap	Euclidean	1	0.073	0.824	5.963	1.039
	Trig-only	1	0.073	0.824	0.000	0.001
	Barrier-only	1	0.073	0.824	5.963	1.039
	Full trig-barrier	1	0.073	0.824	0.000	0.001
Joint-limit grazing	Euclidean	1	0.098	0.431	0.000	0.065
	Trig-only	1	0.098	0.431	0.000	0.065
	Barrier-only	1	0.098	0.431	0.000	0.065
	Full trig-barrier	1	0.098	0.431	0.000	0.065
Near-singular reach	Euclidean	0	0.000	0.851	0.000	0.046
	Trig-only	0	0.000	0.851	0.000	0.046
	Barrier-only	1	0.050	0.608	0.000	0.371
	Full trig-barrier	1	0.050	0.608	0.000	0.371
Combined	Euclidean	0	0.004	0.694	5.883	1.164
	Trig-only	0	0.004	0.694	0.000	0.140

	Barrier-only	0	0.013	0.369	5.883	1.740
	Full trig-barrier	1	0.087	0.590	0.000	0.465

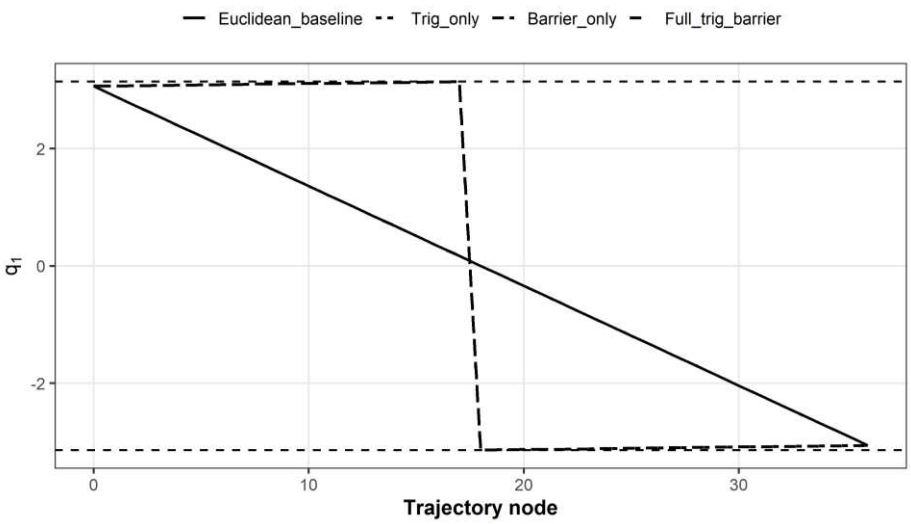


Figure 2. Figure 2. First-joint angular trajectory under $-\pi/\pi$ wrap-around crossing..

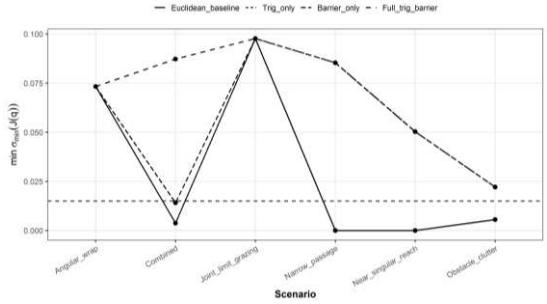


Figure 3. Minimum Jacobian singularity margin across controlled scenarios.

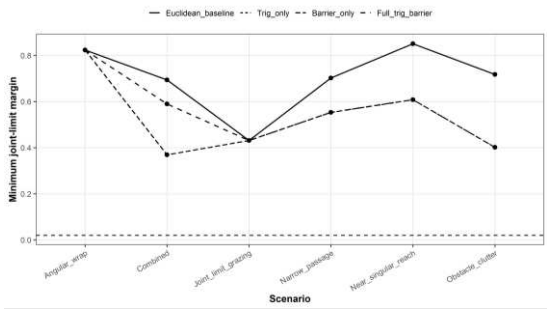


Figure 4. Minimum normalized joint-limit margin across controlled scenarios.

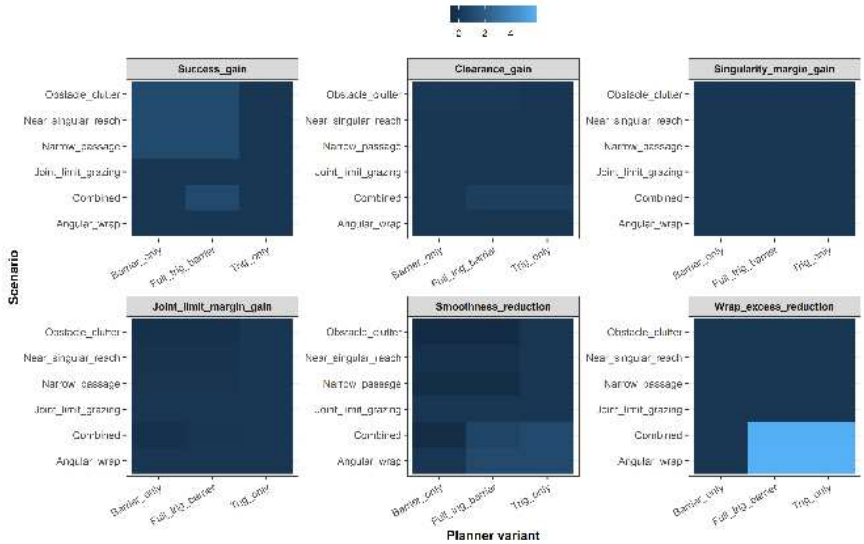


Figure 5. Ablation heatmap of planner gains relative to the Euclidean baseline.

4. Real-Data Periodic-Coordinate Validation

4.1. Recorded-Trajectory Diagnostic Scope

The real-data component used the public LeRobot DROID-100 subset as an offline recorded-trajectory diagnostic layer for the periodic-coordinate part of the proposed framework. DROID is a large-scale in-the-wild robot manipulation dataset introduced by Khazatsky et al. (2024), with demonstrations collected across diverse real-world scenes and manipulation tasks. The DROID-100 subset provides recorded state, action, timestamp, episode-index, and frame-index fields in tabular time-series form. These fields are sufficient for testing whether raw Euclidean angular subtraction produces branch-cut path inflation in recorded robot motion. The analysis was restricted to topology-aware trajectory diagnostics. It did not use reconstructed scene geometry, robot Jacobians, obstacle fields, or manufacturer-certified joint-limit models. Therefore, the DROID-100 results support only the periodic-coordinate component of the framework, while collision avoidance, singularity-margin preservation, and joint-limit safety are evaluated in the controlled simulation layer.

4.2. Periodic Path Inflation

In the DROID-100 diagnostic sample, there are 100 recorded episodes, 32,212 trajectory frames, and 47 task labels, as mentioned in Table 4. Among these paths, 398 raw wrap jumps were identified, with 84 episodes exhibiting an angular wrap discontinuity or more. While the trigonometric shortest-periodic path length was 507.335, the Euclidean periodic-coordinate path length was 2991.414. Under raw Euclidean angular subtraction, this equates to an inflation of 5.896 times.

At the episode level, Figure 6 demonstrates the identical effect. When we use trigonometric shortest-periodic representation, we get compact path-length values, but when we use Euclidean angular subtraction, we get bigger and more scattered path lengths. This finding lends credence to the concept that, in the case of branch-cut crossings, the recorded periodic-coordinate motion can be greatly exaggerated by using Euclidean angular subtraction. It is important to consider both the findings of the paired baseline tests and the statistical comparison when interpreting the data from Appendix Table A2.

4.3. Episode-Level Wrap Excess

The distribution of angular wrap excess at the episode level is displayed in Figure 7. The majority of the episodes that have been recorded have nonzero wrap excess, and the trajectories with large or recurrent branch-cut discontinuities are shown by the upper tail. Recorded robot trajectories can show large fake path inflation when periodic coordinates are evaluated using raw Euclidean subtraction, as shown in Table 4's diagnostic finding.

4.4. Channel-Level Wrap Structure

The channel-level decomposition shows that the wrap effect is concentrated in one periodic motor-state coordinate. Table 4 reports that 397 of the 398 detected wrap jumps occur in channel q_4, while q_5 and q_6 contribute only negligibly. Figure 8 confirms this structure: q_4 has a large Euclidean path accumulation and a much shorter corresponding trigonometric path. This pattern indicates a localized branch-cut effect rather than a uniform artefact across all periodic channels.

4.5. Numerical Consistency of the Trigonometric Embedding

The numerical consistency of the sine-cosine embedding is further confirmed by the recorded trajectories. The highest unit-circle identity error is 2.22×10^{-16} and the maximum chordal-distance identity error is 7.53×10^{-10}, as shown in Table 4. These numbers prove that the trigonometric model keeps the desired periodic geometry exactly as expected. The assertion that trigonometric geometry eliminates branch-cut path inflation in recorded periodic-coordinate robot motion is supported by real-data in Table 4 and Figures 6-8 taken together. Only periodic-coordinate correction has been validated by this data; it does not support claims of success in avoiding collisions, certification of joint limits, avoidance of singularities, or performance of safety filters in real time.

Table 4. DROID-100 real-data periodic-coordinate diagnostics.

Diagnostic quantity	Value	Interpretation
Recorded episodes	100	Real-data diagnostic sample
Recorded frames	32,212	Total trajectory observations
Task labels	47	Heterogeneous manipulation tasks
Episodes with wrap discontinuity	84	Wrap effects occur in most recorded episodes
Raw wrap jumps	398	Euclidean angular subtraction detects many branch-cut jumps
Euclidean periodic-coordinate path	2991.414	Raw coordinate accumulation
Trigonometric periodic-coordinate path	507.335	Shortest-periodic path accumulation
Path inflation factor	5.896	Euclidean subtraction overstates periodic motion
Angular wrap excess	2484.070	Artificial motion removed by trigonometric geometry
Dominant wrap channel	q_4: 397/398 jumps	Wrap inflation is concentrated in one periodic channel
Maximum unit-circle identity error	(2.22×10^{-16})	$(\sin^2(q) + \cos^2(q) = 1)$ holds to numerical precision
Maximum chordal-identity error	(7.53×10^{-10})	Sine-cosine distance identity is numerically stable

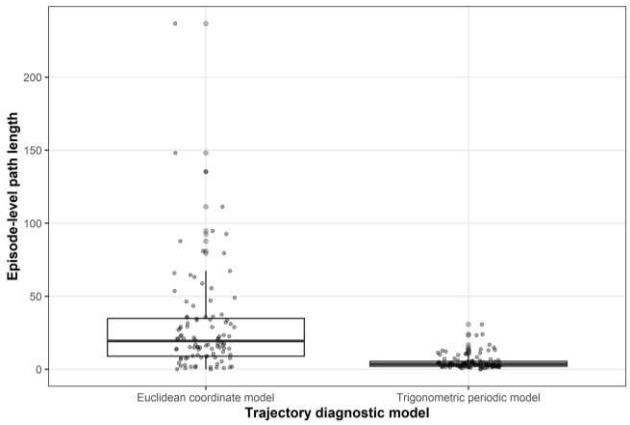


Figure 6. Recorded DROID-100 periodic-coordinate path length under Euclidean and trigonometric models.

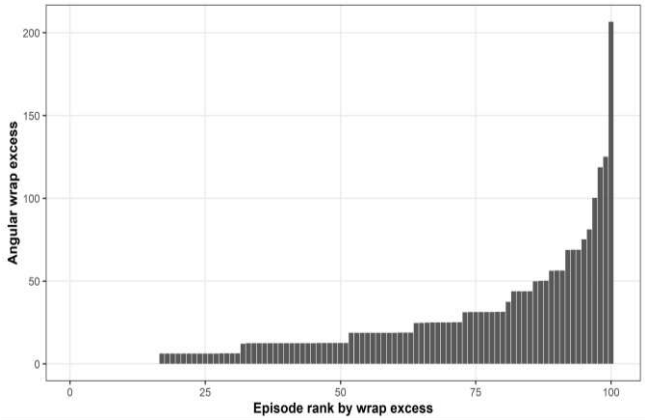


Figure 7. Angular wrap excess across recorded DROID-100 episodes.

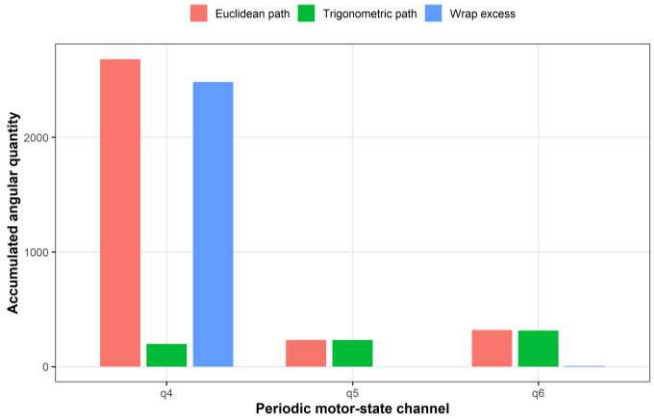


Figure 8. Periodic motor-state channel contribution to wrap correction.

5. Discussion

The results demonstrate that path length, trajectory smoothness, and safety-margin behaviour should not be assessed using periodic robotic coordinates as conventional Euclidean variables. When a trajectory traverses a coordinate branch cut, two angular states that are physically adjacent may appear far away because revolute-joint coordinates are defined modulo 2π. This discrepancy changes the geometry of the planning problem and can cause the robot's apparent motion to be significantly exaggerated. Using tangent barriers for boundary-sensitive safety margins, torus-consistent trajectory smoothness, and sine-cosine angular embedding, the suggested trigonometric barrier formulation tackles this issue.

The controlled simulations reveal distinct roles for the trigonometric and barrier components. A big amount of wrap excess is generated in the angular-wrap case because the barrier-only planner and the Euclidean baseline both take the long coordinate path over the branch cut. In order to restore the shortest periodic motion, the trigonometric-only and full trigonometric-barrier planners eliminate this artefact. This finding lends credence to the paper's central geometric argument: with sine-cosine embedding and a torus-consistent distance, angular motion becomes quotient-consistent.

The singularity experiments reveal an independent process. A trajectory can nevertheless approach a Jacobian-singular configuration even after angular geometry corrections. In the case of approaching the singularity, the trigonometric-only planner and the one based on the Euclidean baseline both collapse, whereas the ones based on barriers alone and the whole trigonometric-barrier both manage to keep a positive singularity margin. The tangent barrier is determined to be the active safety-margin component according to this finding. In order to eliminate periodic-coordinate distortion, one can use the trigonometric distance; for approaching dangerous borders, one can use the tangent barrier. The assertion that topology-aware distance alone ensures safe mobility is unfounded, hence it is best to keep these functions distinct.

The whole formulation is most strongly supported by the coupled constrained situation. Here, safety-margin limitations and angular wrap-around distortion coexist. A big wrap excess and a small singularity margin are both retained by the Euclidean baseline, which causes it to fail. The absence of boundary-sensitive safety penalisation causes the trigonometric-only planner to fail, even after removing the wrap excess. The singularity margin is improved by the barrier-only planner, but the distortion of the Euclidean wrap is retained. The only planner that can do all three things at once—remove wrap excess, keep a positive singularity margin, and maintain joint-limit feasibility—is the full trigonometric barrier planner. This pattern of ablation lends credence to the idea that the suggested technique integrates two supplementary processes: topology-consistent angular motion and margin-aware avoidance of hazardous borders.

A cautious reading is necessary for the joint-limit grazing scenario. There is no clear joint-limit benefit of the suggested technique in this particular scenario since all planner alternatives are feasible. When safety-margin behaviour and periodic-coordinate correction are required to work in tandem, the contribution becomes more apparent in coupled settings. Thus, rather than being consistently better in every single test, the full trigonometric-barrier formulation is best understood as being most beneficial when safety constraints intersect with angular wrap effects.

The DROID-100 analysis backs up the framework's periodic-coordinate component with real-data evidence. The length of the shortest-periodic trigonometric path is 5.896 times less than the length of the Euclidean periodic-coordinate path, and the majority of the recorded episodes include an angular wrap discontinuity. The findings demonstrate that recorded manipulation trajectories are not the only places where branch-cut artefacts can be found; they can also be found in synthetic examples. A localised branch-cut effect, rather than uniform random noise across all channels, is supported by the channel-level decomposition, which further shows that the inflation is concentrated in a single periodic motor-state coordinate.

It is important to interpret the DROID-100 results within the limits of their diagnostic capabilities. Offline periodic-coordinate analysis is supported by the dataset, but certification of collision avoidance, singularity avoidance, joint-limit safety, or real-time safety-filter performance requires calibrated robot geometry, obstacle fields, Jacobians, manufacturer-certified joint-limit models, or closed-loop command data, which are not provided. Thus, the angular-topology part of the framework is validated by the real-data layer, and the safety-margin part is evaluated by the controlled simulation layer under admissibility and geometry constraints that are clearly established.

There is methodological support for the assertion from the algorithmic implementation as well. The finite candidate-search planner employs boundary-biased perturbations, edge-sampled admissibility checks, finite-cost rejection, and shortest-arc interpolation. Since finite-cost nodal safety cannot provide safety throughout segments of continuous motion, these measures are essential. Thus, the edge-sampling condition adds another admissibility check between successive nodes in the trajectory. Rather than being advertised as a one-size-fits-all solution for nonlinear optimal control problems, this implementation offers a repeatable validation method that can be used to compare different types of planning: Euclidean, trigonometric-only, barrier-only, and full trigonometric-barrier.

A limited but significant contribution is established by the study overall. It establishes quotient consistency and boundary divergence for the suggested functional, shows that controlled simulations exhibit complementary ablation behaviour, and verifies on DROID-100 trajectories that recorded periodic-coordinate motion can be significantly inflated by applying Euclidean angular subtraction. A certified hardware-safety system is not the intended use of the framework; rather, it is a mathematically consistent diagnostic and planning layer for robotic systems using periodic configuration spaces. The system should be expanded in future work to include calibrated robot models, certified segment collision checks, dynamic obstacle sensing, latency-aware closed-loop filtering, hardware experiments, and planners for higher-dimensional manipulation tasks that are based on gradients or samples.

6. Real-Time Implementation Pathway

The proposed design is capable of being employed as an intermediary layer for supervision between a low-level robot controller and a nominal motion generator. Artificial discontinuities induced by periodic angular coordinates and inadequate penalisation of motion near obstacle-clearance, joint-limit, or singularity borders are two challenges that need to be solved at the command level before actuation can get underway. The need for robots to maintain a safe distance from people, obstacles, and command-level limits is a common problem in collaborative and field manipulation contexts (ISO, 2016; Khazatsky et al., 2024; Maithani et al., 2026).

To begin a pipeline that is focused on deployment, one must first design a reference trajectory according to Eq. (17), which is a trigonometric planning functional. A tangent barrier discourages the approach to potentially hazardous boundaries, while sine-cosine geometry assesses angular motion. To ensure safety along continuous motion segments, the accepted trajectory must meet both the discrete-cost safety at trajectory nodes and the edge-sampled admissibility criterion in Eq. (21).

Equation (19) then calls for the safety filter to execute the online layer. Nominal command u_t^0 is provided by a tracking controller, task policy, or local planner at every sampling time. By analysing obstacle-clearance, joint-limit, and singularity margins, the filter is able to forecast the subsequent state utilising the local model $F_h(q_t, u)$. No changes are made to the nominal command before transmission if the projected state stays within the safe planning window. When the anticipated state is getting close to a potentially dangerous border, the filter calculates the smallest R-weighted adjustment that brings it back to finite-cost acceptability. The controller suspends operations, rethinks its strategy, or enters a fail-safe mode if no workable solution is found.

The four steps that make up the pathway are as follows: input logging, local command rectification, safety-margin evaluation, and topology-aware state encoding. Interventions prompted by angular wrap exposure, loss of obstacle clearance, proximity to joint limits, or singularity danger are recorded in the logging stage. The ablation design is reflected in this structure: tangent barriers control the distance to dangerous borders, and trigonometric geometry fixes periodic-coordinate measurements.

There is no certification for hardware safety along this deployment-oriented strategy. Validation of periodic-coordinate correction on recorded DROID-100 trajectories and evaluation of safety-margin behaviour in controlled simulation are both carried out in this study. Complete scene-level safety, manufacturer-level joint-limit certification, certified collision avoidance, and ISO compliance are all claims that it does not make. In order to launch a certified deployment, several things must be in place, such as verified collision models, latency and actuator restrictions, dynamic obstacle sensing, emergency-stop integration, safety protocol approval, hardware testing, and robot geometry calibration.

7. Conclusion

An approach to robot motion planning on periodic configuration spaces using trigonometric barrier geometry was proposed in this paper. Although revolute-joint motion is periodic, many planning and diagnostic pipelines still use Euclidean subtraction to determine angular displacement. This work addressed a structural restriction of conventional trajectory models. This technique can inflate path-length or smoothness metrics and create fake branch-cut discontinuities, depending on the chart. This representation is supplanted by sine-cosine embedding and torus-consistent motion measurement in the suggested formulation.

The two mechanisms that make up the framework work together. The tangent-barrier component penalises approach to obstacle-clearance, joint-limit, and Jacobian-singularity boundaries, whereas the trigonometric component gives a quotient-consistent description of angular motion. Their union establishes a safety-margin functional for robotic systems that takes geometry into account, specifically for systems with configuration spaces that contain periodic coordinates.

Quotient consistency, boundary divergence, finite-cost nodal admissibility, interior smoothness, and perturbation stability away from hazardous boundaries were the primary structural aspects of the formulation that were demonstrated by the theoretical study. Based on these features, the implementation created a finite candidate-search planner that includes shortest-arc interpolation, edge-sampled admissibility checks, and a safety-filter pathway for command-level correction in real-time.

Within the specified validation area, the empirical results provide credence to the suggested formulation. Different types of failures are addressed by topology-aware distance and tangent barriers, according to controlled simulations. The distortion of the angular wrap is eliminated by the trigonometric component, and the safety margins close to the singularity and the bounds of the constraints are maintained by the barrier component. Within the coupled limited scenario, the sole planner capable of eliminating wrap surplus while preserving positive singularity and joint-limit margins was the full trigonometric-barrier planner. In addition, the DROID-100 trajectory analysis demonstrated that the trigonometric representation restores the structure of the shortest periodic path, whereas the use of Euclidean angular subtraction can significantly amplify the recorded periodic-coordinate motion.

Not a certified hardware-safety solution, but a mathematically consistent planning and diagnostic layer is what the contribution is supposed to be. Under known geometry and admissibility conditions, the controlled simulations assess safety-margin behaviour, while the real-data analysis confirms periodic-coordinate correction. Automated obstacle detection, physical hardware testing in accordance with established safety standards, validated collision geometry, actuator and delay limitations, and calibrated robot models are all necessary for certified deployment.

In the future, researchers should build on this framework to include scalable gradient-based or sampling-based planners for high-dimensional manipulation systems, dynamic obstacle environments, certified continuous-segment collision checks, calibrated robot trials, and predictive safety filtering using closed-loop models. Trigonometric barrier geometry offers a solid computational foundation for safety-margin motion planning on periodic robotic configuration spaces, under the parameters indicated by this research.

8. Limitations and Future Directions

The proposed framework provides a mathematically consistent planning geometry for robotic systems with periodic configuration spaces. Its validation, however, is limited by the evidence used in this study. Controlled simulations evaluate the behavior of the trigonometric distance, tangent barriers, edge-sampled admissibility, and safety-filter formulation under explicit geometric assumptions. The DROID-100 analysis verifies only the recorded-trajectory effect of angular branch-cut correction. These limits are important because the proposed method is a diagnostic and supervisory planning layer, not a certified hardware-safety system.

i. The safety-margin claims are supported by scenarios with predefined obstacle geometries, joint-limit charts, admissibility criteria, and Jacobian-based singularity margins. This design isolates the mathematical behavior of the proposed functional, but it does not include sensor uncertainty, dynamic obstacles, actuator saturation, latency, contact interaction, emergency-stop integration, or hardware-level safety protocols.

ii. The present implementation uses finite candidate search with edge-sampled admissibility rather than a full nonlinear optimal-control or sampling-based planning architecture. This choice makes the ablation study reproducible and interpretable, but it limits claims about global optimality, computational scalability, and performance in cluttered high-dimensional workspaces.

iii. he DROID-100 results show that Euclidean angular subtraction can inflate recorded periodic-coordinate motion. This evidence does not validate online safety filtering, collision avoidance, joint-limit protection, or singularity avoidance. Those claims require calibrated robot geometry, task Jacobians, collision models, scene-level spatial data, and manufacturer-specified joint constraints.

iv. Future work should integrate the safety filter into a closed-loop command pipeline with specified sampling periods, actuator limits, sensing latency, and infeasible-command recovery rules. Such validation would test whether the correction rule in Eq. (19) can operate as a reliable online supervisory layer rather than only as a deployment-oriented formulation.

v. The current edge-sampled admissibility check improves safety assessment between trajectory nodes, but it remains a sampled verification method. Stronger continuous-motion guarantees

would require certified segment collision checking, signed-distance verification, or reachable-set bounds under bounded tracking error.

vi. A future experimental phase should use a calibrated manipulator model with manufacturer joint limits, measured actuator constraints, reconstructed scene geometry, and real-time logging of safety-filter interventions. Such experiments would allow measurement of computational time, intervention frequency, obstacle-clearance preservation, joint-limit exposure, singularity exposure, and safety-margin behavior during physical robot operation.

Declaration

Contribution: M.H.A. and L.M.A. contributed to the conception and design of the study. M.H.A. developed the main mathematical formulation, including the trigonometric configuration-space representation, tangent-barrier functional, and theoretical properties. L.M.A. contributed to the methodological refinement, simulation design, data organization, and interpretation of the DROID-100 diagnostic analysis. Both authors contributed to validation, interpretation of results, manuscript drafting, critical revision, and approval of the final version.

Data Availability Statement: The recorded robot trajectory data used for the real-data diagnostic analysis are publicly available from the LeRobot DROID-100 dataset hosted on Hugging Face: https://huggingface.co/datasets/lerobot/droid_100. DROID-100 is a tabular/time-series subset associated with the DROID benchmark dataset and contains recorded robot state, action, timestamp, episode-index, and task-related fields used in the present periodic-coordinate diagnostic analysis. The original DROID benchmark is publicly documented by Khazatsky et al. (2024) and through the official DROID dataset resources. No proprietary or privately collected robot data were used in this study.

Funding: The authors received no specific funding for this work.

Competing interests: The authors declare no competing financial or non-financial interests.

References

Ali, U., Wu, L., Mueller, A., Sukkar, F., Kaupp, T., & Vidal-Calleja, T. (2024). Interactive distance field mapping and planning to enable human–robot collaboration. *IEEE Robotics and Automation Letters, 9*(12), 10850–10857. https://doi.org/10.1109/LRA.2024.3482128

Ames, A. D., Xu, X., Grizzle, J. W., & Tabuada, P. (2017). Control barrier function based quadratic programs for safety critical systems. *IEEE Transactions on Automatic Control, 62*(8), 3861–3876. https://doi.org/10.1109/TAC.2016.2638961

Aydogmus, O., & Boztas, G. (2024). Implementation of singularity-free inverse kinematics for humanoid robotic arm using Bayesian optimized deep neural network. *Measurement, 229*, Article 114471. https://doi.org/10.1016/j.measurement.2024.114471

Baron, N., Philippides, A., & Rojas, N. (2020). A robust geometric method of singularity avoidance for kinematically redundant planar parallel robot manipulators. *Mechanism and Machine Theory, 151*, Article 103863. https://doi.org/10.1016/j.mechmachtheory.2020.103863

Brunke, L., Greeff, M., Hall, A. W., Yuan, Z., Zhou, S., Panerati, J., & Schoellig, A. P. (2022). Safe learning in robotics: From learning-based control to safe reinforcement learning. *Annual Review of Control, Robotics, and Autonomous Systems, 5*, 411–444. https://doi.org/10.1146/annurev-control-042920-020211

Cohen, M. H., Molnar, T. G., & Ames, A. D. (2024). Safety-critical control for autonomous systems: Control barrier functions via reduced-order models. *Annual Reviews in Control, 57*, Article 100947. https://doi.org/10.1016/j.arcontrol.2024.100947

Dawson, C., Gao, S., & Fan, C. (2023). Safe control with learned certificates: A survey of neural Lyapunov, barrier, and contraction methods for robotics and control. *IEEE Transactions on Robotics, 39*(3), 1749–1767. https://doi.org/10.1109/TRO.2022.3232542

Elgohr, A. T., Rashad, M., El-Gendy, E. M., Shaaban, W., & Saafan, M. M. (2026). Dynamic quality aware path planning for 6 DoF robotic arms using BiRRT and metaheuristic optimization based on B-spline paths. Scientific Reports, 16, Article 7487. https://doi.org/10.1038/s41598-026-37676-8

Garg, K., Usevitch, J., Breeden, J., Black, M., Agrawal, D., Parwana, H., & Panagou, D. (2024). Advances in the theory of control barrier functions: Addressing practical challenges in safe control synthesis for autonomous and robotic systems. *Annual Reviews in Control, 57*, Article 100945. https://doi.org/10.1016/j.arcontrol.2024.100945

Ghosh, D., Walke, H., Pertsch, K., Black, K., Mees, O., Dasari, S., Hejna, J., Kreiman, T., Xu, C., Luo, J., Tan, Y. L., Chen, L. Y., Sanketi, P., Vuong, Q., Xiao, T., Sadigh, D., Finn, C., & Levine, S. (2024). Octo: An open-source generalist robot policy. In *Robotics: Science and Systems XX*. https://doi.org/10.15607/RSS.2024.XX.090

Hentout, A., Maoudj, A., & Aouache, M. (2023). A review of the literature on fuzzy-logic approaches for collision-free path planning of manipulator robots. *Artificial Intelligence Review, 56*(4), 3369–3444. https://doi.org/10.1007/s10462-022-10257-7

Hewing, L., Wabersich, K. P., Menner, M., & Zeilinger, M. N. (2020). Learning-based model predictive control: Toward safe learning in control. *Annual Review of Control, Robotics, and Autonomous Systems, 3*, 269–296. https://doi.org/10.1146/annurev-control-090419-075625

Hsu, K.-C., Hu, H., & Fisac, J. F. (2024). The safety filter: A unified view of safety-critical control in autonomous systems. *Annual Review of Control, Robotics, and Autonomous Systems, 7*, 47–72. https://doi.org/10.1146/annurev-control-071723-102940

International Organization for Standardization. (2016). *ISO/TS 15066:2016: Robots and robotic devices: Collaborative robots*. International Organization for Standardization.

Khazatsky, A., Pertsch, K., Nair, S., Balakrishna, A., Dasari, S., Karamcheti, S., Nasiriany, S., Srirama, M. K., Chen, L. Y., Ellis, K., Fagan, P. D., Itkina, M., Lepert, M., Ma, J., Miller, P. T., Wu, J., Ha, H., Lee, Y., Wang, K., . . . Levine, S. (2024). DROID: A large-scale in-the-wild robot manipulation dataset. In *Robotics: Science and Systems XX*. https://doi.org/10.15607/RSS.2024.XX.120

Koptev, M., Figueroa, N., & Billard, A. (2023). Neural joint space implicit signed distance functions for reactive robot manipulator control. *IEEE Robotics and Automation Letters, 8*(2), 480–487. https://doi.org/10.1109/LRA.2022.3227860

Li, X., Luo, L., Zhao, H., Ge, D., & Ding, H. (2023). Inverse kinematics solution based on redundancy modeling and desired behaviors optimization for dual mobile manipulators. *Journal of Intelligent & Robotic Systems, 108*, Article 37. https://doi.org/10.1007/s10846-023-01884-5

Li, Y., Chi, X., Razmjoo, A., & Calinon, S. (2024a). Configuration space distance fields for manipulation planning. *arXiv preprint arXiv:2406.01137*. https://doi.org/10.48550/arXiv.2406.01137

Li, Y., Zhang, Y., Razmjoo, A., & Calinon, S. (2024b). Representing robot geometry as distance fields: Applications to whole-body manipulation. In *Proceedings of the IEEE International Conference on Robotics and Automation* (pp. 15351–15357). IEEE. https://doi.org/10.1109/ICRA57147.2024.10611674

Maithani, P., Arab, A., Khorrami, F., & Krishnamurthy, P. (2026). Proactive hierarchical control barrier function-based constraint prioritization to enhance safety in human–robot interaction. Control Engineering Practice, 166, Article 106624. https://doi.org/10.1016/j.conengprac.2025.106624

Narendula, S. T., Bandamidapalli, A., Damodaran, G. V. K., & Rajagopal, P. (2026). Obstacle avoidance for human-centric environments using a modified artificial potential field-probabilistic roadmaps based planner. Journal of Intelligent & Robotic Systems, 112, Article 35. https://doi.org/10.1007/s10846-025-02311-7

O'Neill, A., Rehman, A., Maddukuri, A., Gupta, A., Gupta, A., Padalkar, A., Lee, A., Pooley, A., Gupta, A., Mandlekar, A., Jain, A., Tung, A., Bewley, A., Herzog, A., Irpan, A., Khazatsky, A., Rai, A., Gupta, A., Wang, A., . . . Lin, Z. (2024). Open X-Embodiment: Robotic learning datasets and RT-X models. In *Proceedings of the IEEE International Conference on Robotics and Automation* (pp. 6892–6903). IEEE. https://doi.org/10.1109/ICRA57147.2024.10611477

Orthey, A., Chamzas, C., & Kavraki, L. E. (2024). Sampling-based motion planning: A comparative review. *Annual Review of Control, Robotics, and Autonomous Systems, 7*, 285–310. https://doi.org/10.1146/annurev-control-061623-094742

Ortiz, J., Clegg, A., Dong, J., Sucar, E., Novotny, D., Zollhoefer, M., & Mukadam, M. (2022). iSDF: Real-time neural signed distance fields for robot perception. In *Robotics: Science and Systems XVIII*. https://doi.org/10.15607/RSS.2022.XVIII.012
Secil, S., & Ozkan, M. (2023). A collision-free path planning method for industrial robot manipulators considering safe human–robot interaction. *Intelligent Service Robotics, 16*, 323–359. https://doi.org/10.1007/s11370-023-00465-7
Wabersich, K. P., & Zeilinger, M. N. (2021). A predictive safety filter for learning-based control of constrained nonlinear dynamical systems. *Automatica, 129*, Article 109597. https://doi.org/10.1016/j.automatica.2021.109597
Walke, H. R., Black, K., Zhao, T. Z., Vuong, Q., Zheng, C., Hansen-Estruch, P., He, A. W., Myers, V., Kim, M. J., Du, M., Lee, A., Fang, K., Finn, C., & Levine, S. (2023). BridgeData V2: A dataset for robot learning at scale. *Proceedings of Machine Learning Research, 229*, 1723–1736. https://proceedings.mlr.press/v229/walke23a.html
Zhang, L., Cai, K., Sun, Z., Bing, Z., Wang, C., Figueredo, L., Haddadin, S., & Knoll, A. (2025a). Motion planning for robotics: A review for sampling-based planners. *Biomimetic Intelligence and Robotics, 5*(1), Article 100207. https://doi.org/10.1016/j.birob.2024.100207
Zhang, L., Han, B., Niu, J., Tong, K., Tian, X., Yu, X., Hou, R., & Guo, Y. (2025b). A path planning method based on optimal arm angle of 7-degrees-of-freedom manipulator. *Journal of Intelligent & Robotic Systems, 111*, Article 50. https://doi.org/10.1007/s10846-025-02246-z

Appendix

Table A1. Full simulation configurations and planner variants.

Panel	Item	Role	q_0	q_H	Obstacles	Purpose
A	Angular wrap	Main	(3.062, -0.45,0.32, -0.28,0.22, -0.18,0.10)	(-3.062, -0.45,0.32, -0.28,0.22, -0.18,0.10)	0	Periodic wrap-around continuity
A	Joint-limit grazing	Main	(0.25, -0.70,0.55, -0.40,0.30, -0.20,0.15)	(0.65, -1.45,1.25, -1.10,0.90, -0.65,0.45)	0	Joint-limit protection
A	Near-singular reach	Main	(0.28, -0.38,0.30, -0.22,0.18, -0.12,0.08)	(-.28,0.38, -0.30,0.22, -0.18,0.12, -0.08)	0	Singularity-margin preservation
A	Combined	Main	(3.042,0.70, -0.58,0.42, -0.30,0.18, -0.10)	(-3.042, -0.78,0.62, -0.46,0.33, -0.20,0.12)	4	Coupled wrap, safety, and barrier effects
A	Obstacle clutter	Exploratory	(-0.85,0.72, -0.52,0.38, -0.25,0.18, -0.10)	(0.95, -0.70,0.55, -0.42,0.28, -0.18,0.10)	3	Link-aware obstacle stress test
A	Narrow passage	Exploratory	(-0.95,0.76, -0.56,0.42, -0.30,0.20, -0.10)	(0.95, -0.76,0.56, -0.42,0.30, -0.20,0.10)	4	Narrow-passage stress test
A	Perturbed tracking	Robustness	(-0.70,0.65, -0.50,0.35, -0.25,0.15,	(0.70,-0.65,0.50, -0.35,0.25,	3	Post-perturbation margin diagnostics

			-0.08)	-0.15,0.08)		
B	Euclidean baseline	Comparator	—	—	—	Euclidean smoothness with finite diagnostic safety penalty
B	Trigonometric distance only	Ablation	—	—	—	Torus-consistent smoothness without tangent barriers
B	Tangent barrier only	Ablation	—	—	—	Tangent barriers with Euclidean smoothness
B	Full trigonometric barrier	Proposed	—	—	—	Torus-consistent smoothness with tangent safety barriers

Table A2. Baseline comparison tests for DROID-100 trajectory diagnostics

Comparison	**Test**	**Result to report**
Euclidean path vs trigonometric path	Paired Wilcoxon signed-rank test	Report (p)-value from Table 4
Euclidean full-state increment vs topology-aware increment	Paired Wilcoxon signed-rank test	Report (p)-value from Table 4
Euclidean smoothness vs trigonometric smoothness	Paired Wilcoxon signed-rank test	Report (p)-value from Table 4